JGR Oceans

RESEARCH ARTICLE
10.1029/2019JC015646

Key Points:
- Kinetic energy is a proxy for mixed layer depth, operating as a necessary but not sufficient condition for phytoplankton blooms
- High kinetic energy appears to suppress phytoplankton blooms in the Southern Ocean
- The spatial pattern of kinetic energy in the Southern Ocean explains up to 30% of the variability in the spatial distribution of chlorophyll

Supporting Information:
- Supporting Information S1

Correspondence to:
J. C. Gradone,
jgradone@udel.edu

Citation:
Gradone, J. C., Oliver, M. J., Davies, A. R., Moffat, C., & Irwin, A. (2020). Sea surface kinetic energy as a proxy for phytoplankton light limitation in the summer pelagic Southern Ocean. *Journal of Geophysical Research: Oceans*, *125*, e2019JC015646. https://doi.org/10.1029/2019JC015646

Received 11 SEP 2019
Accepted 3 MAR 2020
Accepted article online 10 MAR 2020

Sea Surface Kinetic Energy as a Proxy for Phytoplankton Light Limitation in the Summer Pelagic Southern Ocean

J. C. Gradone[1], M. J. Oliver[1], A. R. Davies[2], C. Moffat[1], and A. Irwin[3]

[1]School of Marine Science and Policy, University of Delaware, Lewes, DE, USA, [2]Oceanography Department, United States Naval Academy, Annapolis, MD, USA, [3]Department of Mathematics and Statistics, Dalhousie University, Halifax, Nova Scotia, Canada

Abstract The pelagic Southern Ocean is a high-nutrient, low-chlorophyll ecosystem. Here, phytoplankton growth is colimited by iron supply and light availability. This creates a general expectation that when light is available in the austral summer (shallow mixing depths), phytoplankton concentrations may be high or low depending on the delivery of iron to the surface layer. When light is not adequate (deep mixing depths), phytoplankton concentrations will likely be low, even if iron is available. Here we show that low surface kinetic energy behaves like a necessary but not sufficient condition for high chlorophyll concentrations. In high kinetic energy conditions, high chlorophyll concentrations are rare. Conversely, under low kinetic energy conditions, both high and low chlorophyll concentrations were observed. We show that higher kinetic energy conditions are related to deeper mixed layers, which is likely a proxy for local light conditions. Probabilistic models of chlorophyll based on surface kinetic energy were able to describe 30% of the spatial variability in monthly chlorophyll climatologies. This means that local light availability, proxied by mixing through kinetic energy, significantly shapes the spatial distribution of chlorophyll in the Southern Ocean. We suggest that regions with consistently higher kinetic energy may not be as sensitive to iron inputs compared to historic iron addition experiments, which were conducted in low surface kinetic energy conditions.

Plain Language Summary Phytoplankton are at the base of the food web in most ocean ecosystems. In the Southern Ocean, they are critical for converting carbon dioxide into organic matter. Some of that organic matter is exported to the deep ocean and sequestered from the atmosphere. Therefore, factors that affect phytoplankton concentrations are important for understanding their impact on both marine ecology and global carbon budgets. Here we show that surface kinetic energy may be an important indicator of phytoplankton concentrations in the Southern Ocean. We propose that increased surface kinetic energy results in deeper vertical mixing, limiting phytoplankton access to light. We show that phytoplankton blooms are not common in high kinetic energy environments in the Southern Ocean in the summertime.

1. Introduction

The pelagic Southern Ocean (SO) is an important region for the global carbon cycle as it takes up approximately 40% of the total anthropogenic carbon that enters the ocean (Gruber et al., 2009). The SO is a high-nutrient, low-chlorophyll (HNLC) region where surface waters are typically macronutrient (e.g., nitrogen and phosphorous) rich during the growing season, yet phytoplankton patterns are highly patchy within a generally unproductive environment (Arrigo et al., 2008; Moore & Abbott, 2000; Venables & Moore, 2010). This patchy distribution is attributed to deficient iron concentrations in the surface waters (Martin, 1990), which can be temporarily alleviated through various mechanisms including eolian deposition, mesoscale eddies, vertical mixing, upwelling, northward advection of iron rich waters, and interactions with nearby fronts (Blain et al., 2001; Boyd & Ellwood, 2010; Comiso et al., 1993; Holm-Hansen et al., 2005; Klunder et al., 2014; Nolting et al., 1991; Song et al., 2018; Uchida et al., 2019; Venables et al., 2007). Because iron is the limiting nutrient for open ocean phytoplankton, SO waters have been the focus of several successful, artificial iron enrichment experiments (Boyd et al., 2000; Coale et al., 2004; Gervais et al., 2002; Hoffmann et al., 2007; Smetacek et al., 2012). Furthermore, iron has also been confirmed to be critical for naturally

occurring phytoplankton blooms within HNLC regions (Blain et al., 2007; Holeton et al., 2005). However, despite the number of studies demonstrating the importance of iron to phytoplankton abundance, light availability, mediated by changes in mixing depth, sets the upper limit of phytoplankton abundance even after relieving iron limitation (Boyd et al., 2000; De Baar et al., 2005).

Conceptually, both light availability, modulated by the mixed layer depth (MLD), and iron concentrations emerge as necessary but not sufficient conditions for phytoplankton blooms in the SO. This condition leads to two probabilistic expectations. When light is available (shallow MLD), the phytoplankton concentrations may be high or low, depending on the delivery of iron to the surface layer through various delivery mechanisms. When light is not adequate (deep MLD) phytoplankton concentrations will likely be low, even if iron is available. Assuming that neither MLD or iron delivery are spatially random in the study area (south of 55°S), these probabilistic relationships resolved in space ought to show where in the pelagic SO iron delivery is more likely to generate high phytoplankton concentrations and where it is less likely due to localized light limitation through increased mixing.

In this manuscript we propose that the relationship between surface mean kinetic energy per unit mass (KE) and mean surface chlorophyll concentration (CHL) is a proxy for the expected probabilistic relationship between light limitation and phytoplankton concentrations in the summertime pelagic SO. To do this, we show empirically that low KE behaves like a necessary but not sufficient condition for high CHL. We then develop a probabilistic model to show that KE is predictive of CHL in the SO, which is validated by in situ observations of CHL by Southern Ocean Carbon and Climate Observations and Modeling (SOCCOM) biofloats. We suggest that high KE values are a proxy for vertical mixing and potentially a deepening mixed layer, causing localized light limitation. Applying the probabilistic model over a 15-year time series of satellite-derived CHL and KE in the SO suggests that up to 30% of the spatial variability in phytoplankton biomass is likely due to local deepening of the mixed layer. Based on our analysis, we also suggest the regions of the pelagic SO that are more likely to result in elevated CHL when iron is added to the surface layer.

2. Materials and Methods

2.1. SO Satellite Chlorophyll Concentrations

Estimates of pelagic SO CHL were made using the National Aeronautics and Space Administration's (NASA) Moderate Resolution Imaging Spectroradiometer (MODIS-Aqua). Standard NASA processing flags were used to remove remote sensing reflectance data in the SO for a failure in atmospheric or aerosol corrections, cloud or ice contamination, and high solar zenith (Esaias et al., 1998). The standard OC3 CHL algorithm for the MODIS-Aqua satellite significantly underestimates CHL at high latitudes (Cota et al., 2003; Dierssen & Smith, 2000; Gregg & Casey, 2004; Kahru & Mitchell, 1999; Strutton et al., 2011). To correct for this, we applied a SO specific CHL algorithm (Johnson et al., 2013). This algorithm is

$$CHL = 10^{\left(0.6994-2.0384R_{MA}-0.4656R_{MA}^{2}+0.4337R_{MA}^{3}\right)}, \quad (1)$$

$$R_{MA} = log10\left(\max\left(Rrs_{\left(\frac{443}{555}\right)}, Rrs_{\left(\frac{490}{555}\right)}\right)\right), \quad (2)$$

where Rrs is remote sensing reflectance (sr^{-1}) at their respective wavelengths (443, 490, or 555 nm). R_{MA} indicates that the algorithm uses $\log_{10}$ of the largest of the two wavelength ratios. Using this algorithm, the dynamic range of CHL increased by 138% (Johnson et al., 2013).

Five-day composites of CHL were made from daily, 9-km resolution, Level 3 remote sensing reflectance data to match to the 5-day composites of KE estimates described in section 2.2. To focus on the pelagic SO, spatial masks were applied to eliminate the higher CHL concentrations caused by islands and shallow coastal waters (Moore & Abbott, 2000; Sokolov & Rintoul, 2007) (Figures 1a and S1 in the supporting information). Only data from December, January, and February (austral summer) were considered in this study because roughly 75% of the satellite CHL estimates came from this season due to reduced cloud cover.

2.2. SO Kinetic Energy Estimates

KE estimates were derived from the National Oceanic and Atmospheric Administration's (NOAA) unfiltered, 1/3° resolution, 5-day-averaged Ocean Surface Current Analysis Real-time (OSCAR) data product.

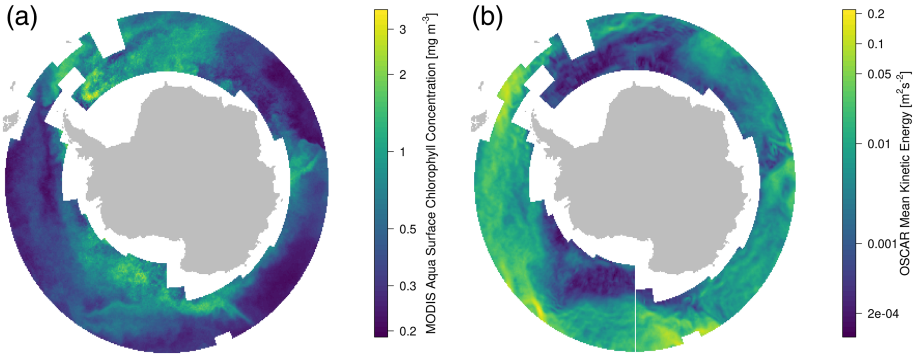

Figure 1. (a) Averaged MODIS-Aqua surface chlorophyll concentration and (b) averaged kinetic energy estimates derived from OSCAR surface currents from 2003–2017 (December–February). These data were masked to avoid the effects of land.

OSCAR surface currents are computed by combining a quasi-steady geostrophic model with wind-driven ageostrophic currents and thermal wind adjustments (Bonjean & Lagerloef, 2002). These currents are representations of spatially and temporally averaged flow over the upper 30 m of the ocean and are calculated by

$$if\overline{\mathrm{U}} = -\mathrm{g}\nabla\varsigma + \frac{\mathrm{h}}{2}\nabla\theta + \frac{\tau - \mathrm{AU}'(-\mathrm{h})}{\mathrm{h}}, \tag{3}$$

where $\overline{U}$ is the horizontal velocity vector, $U(x,y,z,t) \equiv u + iv$, where the bar represents averaged velocity over the upper 30 m. $\nabla \equiv \partial/\partial x + i\partial/\partial y$, where the vector wind stress field divided by the characteristic density is represented by $\tau = \tau^x + i\tau^y$. g is the gravitational constant, ζ is the displacement of the ocean-atmosphere interface, θ is the buoyancy force proportional to∇ (sea surface temperature), f is the Coriolis parameter, and A is the depth-uniform eddy viscosity that characterizes turbulent vertical mixing. $U' \equiv U_z$ denotes the vertical shear, which is assumed to be equal to τ/A at the surface of the ocean and equal to zero at a depth of 30 m (Bonjean & Lagerloef, 2002). The first term on the right-hand side of this equation, $-g\nabla\varsigma$, represents the pressure gradient force, which is adjusted by the contribution of the buoyancy gradient, $(h/2)\nabla\theta$. The last term represents the net drag force applied by the wind stress to depth h.

OSCAR uses a variational analysis of Special Sensor Microwave Imager (SSM/I) winds by Atlas et al. (1996) to compute surface winds with the wind stress vectors being computed using the drag relationship used by Large and Pond (1981). OSCAR also incorporates Jason-1 and Envisat altimetry data. The data are packaged as discrete, temporal blocks of 5-day-averaged currents, from which KE estimates are computed,

$$KE = \frac{1}{2}\left(u^2 + v^2\right), \tag{4}$$

where u and v are the meridional and zonal components of the OSCAR currents, respectively.

Mesoscale dynamics in the SO occur on the order of 75–100 km spatially (Chelton et al., 2007) and 10 days temporally (Daniault & Ménard, 1985). With a 1/3° spatial resolution and a 5-day sampling period, the OSCAR currents are on the same order of magnitude as these features. These data were also masked to avoid the influence of land and island effects (Figure 1).

2.3. Argo Float MLD Climatology

While there are several global MLD products available, there are large uncertainties in the SO component of these products (Dong et al., 2008). Dong et al. (2008) used over 42,000 Argo float profiles of temperature, salinity, and pressure from July 2001 to September 2006 in the SO (30–65°S, 0–360°E) to create a MLD climatology. This monthly climatology is mapped onto a 1° × 1° grid. Dong et al. (2008) defined the MLD as a potential density difference from the surface of 0.03 kg m^{-3} for the SO.

For use in this study, a time-weighted mean of this monthly climatology was created and matched to the corresponding days of the month containing the 5-day-averaged OSCAR currents and MODIS CHL

observations. For spatially coincident estimates of CHL, KE, and MLD in the pelagic SO, the CHL and MLD products were spatially interpolated onto the OSCAR 1/3° × 1/3° grid and restricted to South of 55°S.

2.4. SOCCOM Float Observations

The SOCCOM program has deployed biogeochemical sensors on profiling floats in the SO since 2014. This program is focused on the SO's impact on carbon budget, ocean biogeochemistry, and climate change (Gray et al., 2018). In addition to the temperature, salinity, and pressure sensors, these floats carry oxygen, nitrate, pH, chlorophyll fluorescence, and optical backscatter sensors (Johnson et al., 2017). These floats collect data by profiling the water column from their maximum depth, between 1,400 and 2,000 m, before returning to the surface every 10 days (Johnson et al., 2017). Measurements are only made during ascents and are transmitted via the Iridium satellite network after surfacing. Depth sampling resolution is highest (1.5 m) in the upper 100 m but decreases at greater depths.

At the time of this analysis, there were 76 floats (~3,400 profiles) with quality-controlled and adjusted data that had been in the water for at least 6 months in the SOCCOM database. Approximately 75% of the satellite CHL estimates come from the summer due to the reduced cloud cover during this season. As a result, only summer profiles were used in this study. After removing floats that did not have working fluorometers, applying the land and island masks in Figure 1, and removing the nonsummer profiles, 266 profiles from 31 different floats from 2014 to 2017 were used in this study. Before our analysis of the relationship between KE and CHL, we checked if satellite-derived CHL approximated SOCCOM in situ CHL. A Model II regression showed there was a significant positive relationship (slope = 0.76, intercept = −0.13, r^2 = 0.66, $p << 0.001$) between matched satellite-derived estimates of CHL and mean in situ chlorophyll measurements in the upper 10 m from SOCCOM floats in $\log_{10}$ space (Figure S3). This indicates that the SO specific CHL algorithm (equation 1) does a satisfactory job of representing in situ CHL. These results differ from those reported by Haëntjens et al. (2017) because this study is focused on regions far from land influences.

The surfacing locations of the floats were matched with the nearest satellite observation in a 5 day and 15 km window for comparison. MLDs for each float profile were computed using the potential density difference of 0.03 kg m^{-3} from the surface used in the Dong et al. (2008) study to enable comparison of MLDs from different sources. In situ density profiles were visually inspected with the corresponding computed MLDs to confirm this method's accuracy.

2.5. Kinetic Energy-Chlorophyll Probabilistic Model Development

Fifteen years (2003–2017) of KE and CHL data were matched and parsed by month (December, January, and February). For each month, KE was divided evenly into 10 bins, each containing 10% of the matched data. To model the distributional relationship between KE and CHL, an expectation maximization (EM) algorithm was used to fit a mixture of univariate normal distributions to the observed CHL data in each of the 10 KE bins (Benaglia et al., 2009). Kolmogorov-Smirnov (KS) tests were used to determine if the frequency distributions of satellite-derived CHL observed in each of the 10 KE bins statistically differed from one another (R Development Core Team, 2017).

An EM algorithm is an iterative method to isolate maximum likelihood estimates of parameters for a mixture of two normal distributions describing an observed distribution. The EM algorithm is a two-step process, consisting of an expectation (E) step and a maximization (M) step. This algorithm uses the current parameter estimates to create a function for the expected log likelihood, computes new parameters to maximize the expected log likelihood, and continues to iterate until the log likelihood is effectively maximized (Benaglia et al., 2009). The EM algorithm estimates the means, standard deviations, and mixing percentages for two normal distributions that together approximate the CHL distributions in the 10 KE bins in each month (December–February). These EM estimates were then used as seed values in a nonlinear least squares model to estimate the nonlinear relationship between these mean, standard deviation, and mixing percentage curves for the two distributions as a function of KE (R Development Core Team, 2017). Then, using the function rnormmix in R to simulate from a mixture of univariate normal distributions, these continuous functions were used to probabilistically predict CHL for each KE estimate (Benaglia et al., 2009). This procedure was performed separately for December, January, and February.

2.6. Kinetic Energy-Chlorophyll Probabilistic Model Testing

The parameters for these monthly models were trained on a random 80% of the matched KE-CHL data from each month over the study period and tested on the remaining 20% of the data from each month. Using the R package lmodel2, a Model II ranged major axis (RMA) linear regression was performed to first assess the accuracy of the predicted binned mean and standard deviation of CHL against the observed binned mean and standard deviation of CHL, and for examining the relationship between climatologies of observed and predicted CHL (Legendre, 2014). The probabilistic models were also evaluated spatially by comparing maps of averaged observed and predicted CHL over the 2003–2017 study period.

2.7. Evaluating the Relationship Between Kinetic Energy, MLD and Chlorophyll

The role of KE as a proxy for MLD and CHL concentration was evaluated in both the remotely sensed and in situ data sets. The same 10% binning procedure performed in the development of the monthly probabilistic models was performed on a data set of matched KE, CHL, and MLD from the Argo float climatology. This same procedure was also performed on a SOCCOM float data set of individual profile MLD and CHL matched to KE but with 20% bins because of the smaller sample size from the SOCCOM floats. One-way analysis of variances (ANOVAs) was used to test the impact that different levels of KE had on (remotely sensed and individual profile) MLD and CHL (R Development Core Team, 2017).

3. Results

3.1. Kinetic Energy as a Proxy for MLD

Figure 8 shows the relationship between MODIS-Aqua CHL, OSCAR KE, and climatological MLD throughout the entire SO in all summer months combined and separately in December, January, and February from 2003–2017. The 10 points in each panel of Figure 8 correspond to the same KE bins, each containing 10% of the data described in Figure 3.

Our analysis suggests that high KE is a proxy for deeper MLDs and lower CHL. One-way ANOVAs indicate that mean KE had a statistically significant effect on MLD and CHL (both p values $<< 0.001$). The in situ measurements from the SOCCOM floats show similar results, which confirm what is observed in the remotely sensed data. The same relationship observed in Figure 8 can be seen in Figure 9 but with SOCCOM CHL, MLD, and KE, in December, January, February, and in these months combined. In all the months combined, the one-way ANOVAs indicate that mean KE had a statistically significant effect on the individual profile MLD and CHL (both p values $<< 0.001$).

3.2. Kinetic Energy and Chlorophyll Relationship

Throughout the entire pelagic SO, high levels of KE correspond with low CHL, while high CHL occur at lower KE (Figures 1 and 2). This pattern is consistent when observations are broken down by month (December, January, and February) and is also observed in the in situ SOCCOM float observations (Figure 2), indicating that the general relationship is not an artifact of satellite observations.

One explanation for the lack of high CHL values at high KE is a possible sampling bias. If both high KE and high CHL are rare, these two conditions may not be represented in the data. To confirm that this KE-CHL relationship is not due to a sampling bias, the 15 years of matched KE and CHL data were sorted by KE and then divided into 10 KE bins each containing 10% of the total data. If the pattern is due to sampling bias, these distributions would be self-similar (i.e., show similar statistical properties at many scales). However, when the data are parsed by month, these distributions are not self-similar. KS tests revealed that every distribution of CHL in the KE bins are significantly different from one another ($p << 0.001$). Furthermore, these distributions also provide evidence that there is a seasonal component to this KE-CHL relationship (Figure 3). As the austral summer season progresses from December to February, higher CHL shoulders form in the distributions occurring in the lower KE bins, while the CHL distribution in higher KE bins shifts to lower values.

The results of the EM algorithm show that these distributions can be modeled using a mixture of two normal distributions. These two distributions mix together in difference percentages to represent the observed distribution. We nominally label these the “background” and “bloom” distributions, only to denote that one

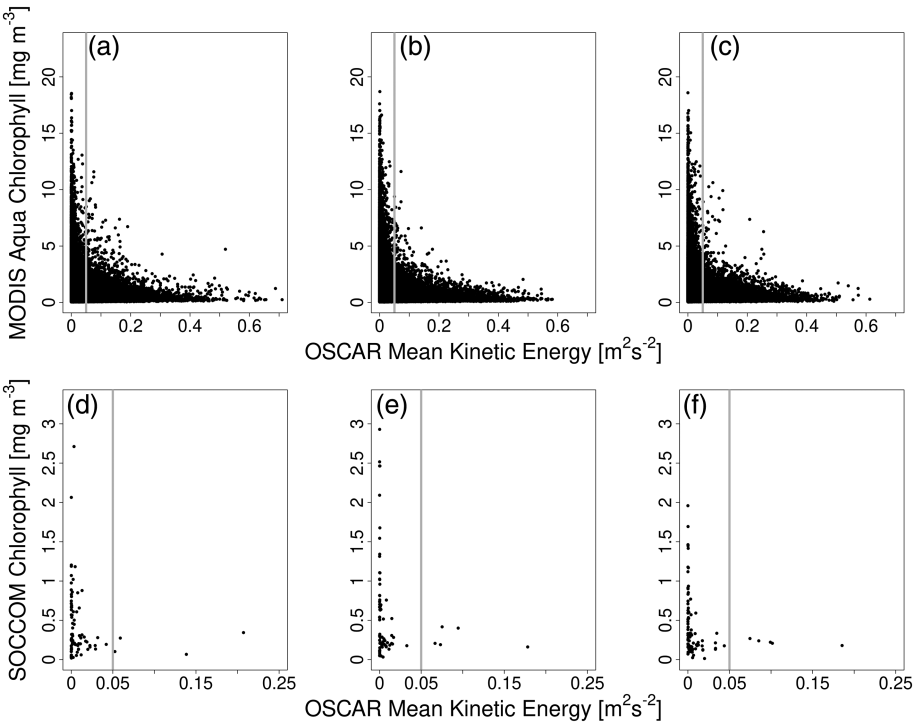

Figure 2. Mean surface kinetic energy and mean surface chlorophyll concentration relationship broken down by month in the remotely sensed and in situ float data sets (December = panels a and d; January = panels b and e; February = panels c and f). Gray bars are for visual reference to show transition from low to high KE regimes (0.05 $m^2\ s^{-2}$).

distribution has a higher mean than the other. The means, standard deviations, and mixing percentages of these two distributions (Figure 4) are fit to either linear or hyperbolic functions of KE:

$$\text{Linear Fit:}Mean, SD, Mix\% = A^*KE + B, \tag{5}$$

$$\text{Hyperbolic Fit:}Mean, SD, Mix\% = \frac{A}{(B + KE)} + C. \tag{6}$$

The mixing percentages of the background and bloom distributions in January and February fit a hyperbolic model. However, this is not the case in December, in which there is no clear function that seems best to approximate the mixing percentages of the background and bloom distribution; therefore, the mixing percentage for these two distributions across different levels of KE is held constant (Table S1). There is also no clear higher CHL shoulder at low KE present in December (Figure 3a), suggesting that the mixing percentage of these background and bloom distributions would have little effect on the model. The coefficients found to fit these functions can be found in Table S1. These estimates of the mean, standard deviation, and mixing percentage for the background and bloom distributions are then used to probabilistically predict CHL from KE in the SO for the pooled observations for December, January, and February from 2003–2017.

To test the performance of these monthly probabilistic KE-CHL models, the models were fit on a random 80% of the pooled data from each month and tested on the remaining 20%. Because these are probabilistic models designed to predict the distribution of CHL based on 5-day composites of KE estimates alone, we compared the observed and predicted mean, standard deviation, and CHL distributions for each of the 10 KE bins for December, January, and February. Model II regression results comparing observed and modeled KE binned CHL means are not significantly different than a 1:1 line for January and February (January Major Axis [MA] regression slope = 1.03, 95% CI = 0.98–1.07 and February MA regression slope = 0. 96, 95% CI = 0.88–1.06; Figure 5a). The regression results for December is significantly different from a 1:1

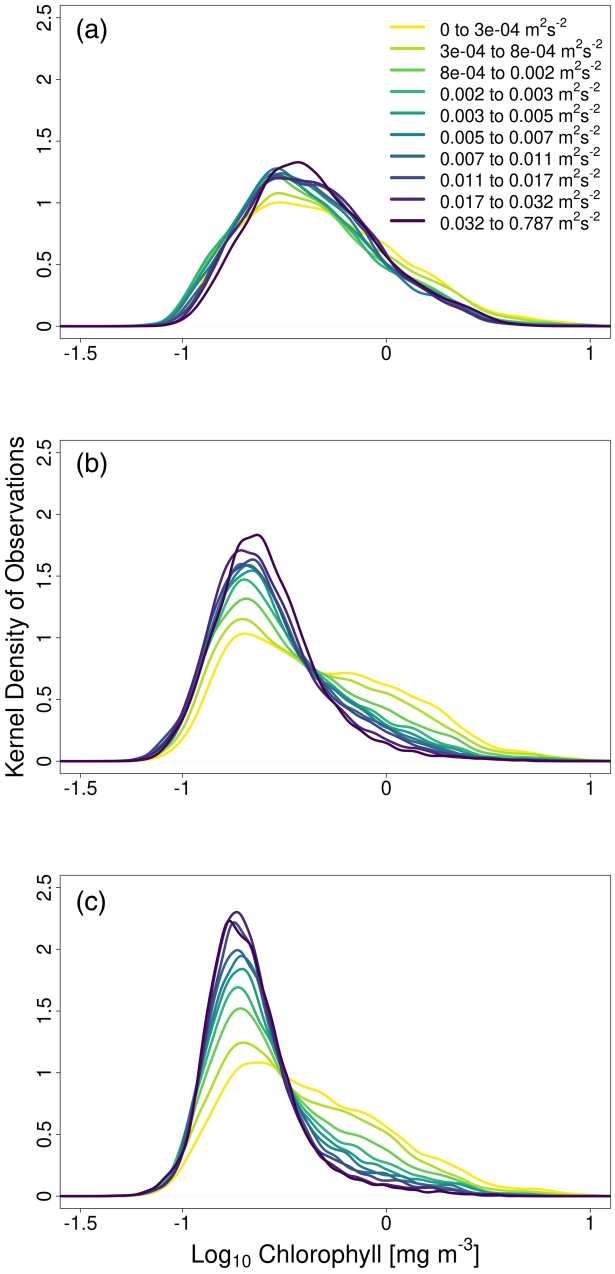

Figure 3. Kernel density distributions of binned MODIS-Aqua surface chlorophyll concentration with coincident OSCAR surface current derived kinetic energy estimates. Each distribution (different colored line) contains 10% of the data for a given month (December, January, and February represents a, b, and c, respectively). High CHL (e.g., 1–10 mg m^{-3}) is more frequent in low KE conditions in January and February.

line (MA regression slope = 0.52; Figure 5a); however, the dynamic range of mean CHL data in December is very small, and therefore, the slope is difficult to estimate. Still, the overall predicted mean is within less than 1% of the observed mean in December. Model II regression including all summer months was not significantly different than a 1:1 line (MA regression slope = 0.99, 95% CI = 0.96–1.03) (Figure 5a).

Model II regression results comparing the observed and modeled KE bin CHL standard deviations are not different than a 1:1 line for December, January, and February (December MA regression slope = 1.19, 95% CI = 0.99–1.35; January MA regression slope = 1.03, 95% CI = 0.96–1.09; February MA regression slope = 0.94, 95% CI = 0.88–1). Model II regression including all months was not significantly different than a 1:1 line either (MA regression slope = 0.98, 95% CI = 0.94–1.02) (Figure 5b).

After comparing the observed and predicted mean and standard deviation for each of the 10 KE bins in each month, the distributions produced from probabilistic models were compared against the observed distributions (Figure 6). The predicted December distribution exhibits higher mean CHL in each bin and is more normally distributed than the January and February distributions, as seen in the observed December distribution (Figures 6a and 6b). The predicted January and February distributions exhibit the same higher CHL shoulders (i.e., higher probability of higher CHL values) in the lower KE bins and lower CHL values in the higher KE bins, as seen in the observed January and February distributions, indicating that these probabilistic models accurately recreate the distributional relationship between KE and CHL (Figures 6c–6f).

Figure 7 shows a comparison of monthly MODIS-Aqua CHL climatologies from 2003–2017 and the monthly climatologies produced by the KE-CHL probabilistic models. A regression analysis of these data sets reveals that, in all the months combined, probabilistic predictions of CHL based on KE alone can explain 30% of the observed spatial variability in phytoplankton abundance (RMA regression slope = 0.323, intercept = −0.139, $R^2 = 0.300$; see Figure S4). In January and February, these models explain 19% and 23% of the observed spatial variability in phytoplankton abundance (RMA regression slope = 0.397, 0.459 and intercept = −0.115, −0.147, $R^2 = 0.186$, 0.234, respectively). The regression between the climatologies of observed and predicted CHL in December is not significant ($R^2 = 0.002$). This is to be expected as the dynamic range of CHL in December is very small (i.e., low binned CHL standard deviation in Figure 4) and KE does not have a statistically significant effect on CHL (Figure 3), likely because the system is undergoing the alleviation of seasonal light limitation.

4. Discussion

Throughout the SO, the highest CHL is typically associated with coastal waters, areas of sea ice retreat, and in the vicinity major frontal systems (Moore & Abbott, 2000). High CHL is also associated with downstream island effects or where the Antarctic Circumpolar Current interacts with bathymetric features (Sokolov & Rintoul, 2007). The focus of this study is on phytoplankton in the pelagic SO, far from the influence of coastal systems and islands. In this region, it has been demonstrated that phytoplankton are mostly limited by the availability of iron (De Baar et al., 2005). The mechanisms that deliver iron to the pelagic SO are varied. The combination of upwelling and vertical mixing of iron rich waters, iceberg meltwater, eolian deposition, and other mechanisms (Boyd & Ellwood, 2010; Boyd et al., 2012; Smith

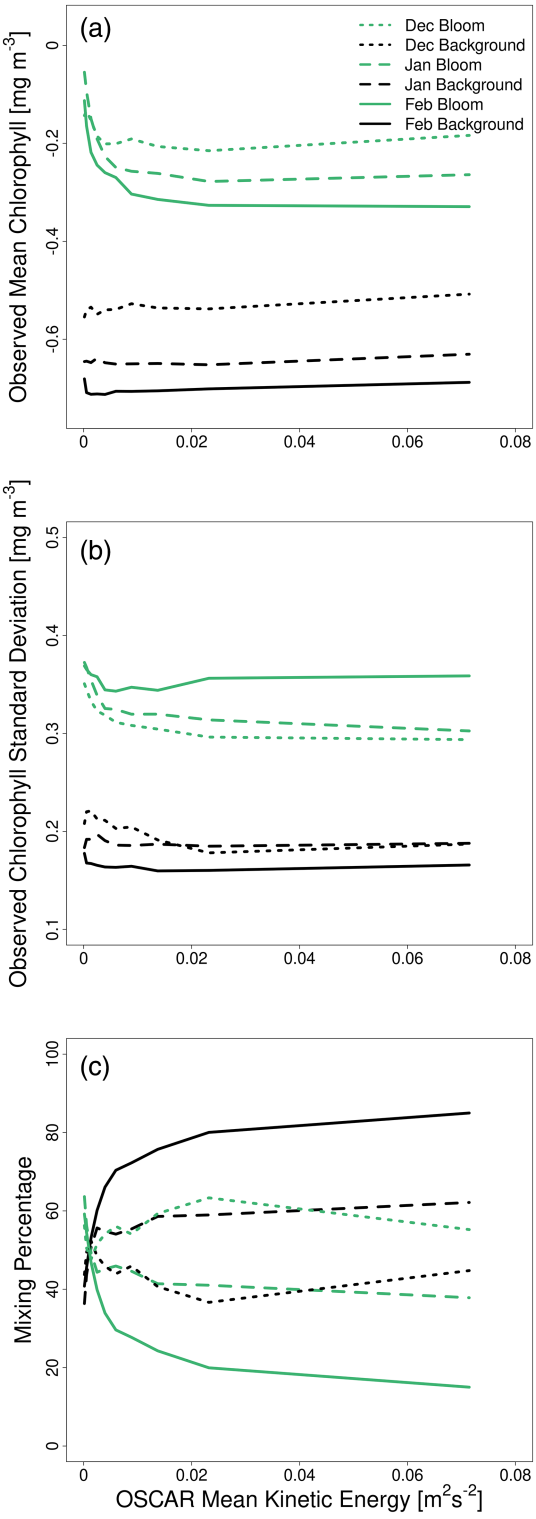

Figure 4. Log_{10} mean (a), standard deviation (b), and mixing percentage (c) of the two distributions (bloom in green and background in black) describing the observed distribution in December (dotted line), January (dashed line), and February (solid line) as a function of mean surface kinetic energy.

et al., 2007; Tagliabue, Sallee, et al., 2014) creates a complex iron delivery system to the surface ocean. Although stochastic in time, the spatial distribution of iron supply to the pelagic SO is not spatially random. Iron supply is generally higher south of the Southern Antarctic Circumpolar Current Front (Boyd et al., 2012).

Overlaid on the complexity of iron delivery is local light availability. Although the pelagic SO is light-limited in seasonal time scales (El-Sayed et al., 1983), light during the growing season can limit the phytoplankton response to iron availability (Boyd et al., 2000). While it has been hypothesized that annual integrated CHL in the HNLC SO is not constrained by light (Venables & Moore, 2010), the generally inverse KE-CHL relationship observed here is likely due to unfavorable light conditions due to locally deeper mixed layers. The differences between this study and Venables and Moore (2010) studies could be due to their coarse temporal and spatial scales (>5° longitude and latitude and one mean estimate of MLD during the summer). Interestingly, Venables and Moore (2010) acknowledge that light levels above a significant threshold are a necessary but not sufficient precondition for bloom development. Using wind speed as a proxy for mixing, Fitch and Moore (2007) demonstrated that phytoplankton blooms were more frequent at lower wind speeds (a proxy for shallow mixing depths) in marginal ice zones, which is a region covered in this analysis. Conversely, as wind speed increased (a proxy for deep mixing depths), blooms were less likely, which was interpreted as light limitation of phytoplankton populations. Using wind speed as a proxy for mixing, Carranza and Gille (2015) found that high wind speeds on daily time scales correlated with increased CHL due to transient MLD deepening and consequent Fe entrainment. While Carranza and Gille (2015) highlight a potentially important Fe supply mechanism, they noted that wind speeds were high enough to transiently deepen MLD and entrain Fe without completely eroding the seasonal MLD, which would expose phytoplankton to a light limited environment. Areas where transient MLD deepening does not coincide with increased CHL are likely locations where newly mixed waters lack bioavailable Fe (Carranza & Gille, 2015). The probabilistic analysis presented here does not rule out or necessarily contradict any of these mechanisms. In fact, the highest peaks of the KE distributions in Figure 3b suggest that as KE increases, there is a slight increase in background CHL distribution in January. However, the overall observed pattern in Figure 3 suggests that low KE is associated more frequently with high CHL values. The effect of mixing on grazing rates is also something this study cannot address. The deepening of the mixed layer may reduce contact rates between grazers and phytoplankton, allowing phytoplankton biomass to increase because of reduced grazing pressure increase (Behrenfeld, 2010). However, our observations indicate that increased mixing due to high KE and deeper mixed layers suppress, rather than enhance CHL. Therefore, these data do not indicate that relaxed grazing pressure due to increased mixing explains the observed relationship between KE and CHL in this study.

4.1. Low Kinetic Energy as a Necessary but Not Sufficient Condition for High Chlorophyll

High CHL is only associated with low KE while low CHL is associated with a broad range of KE magnitudes in both satellite-derived and SOCCOM CHL (Figure 2). However, low KE does not guarantee high

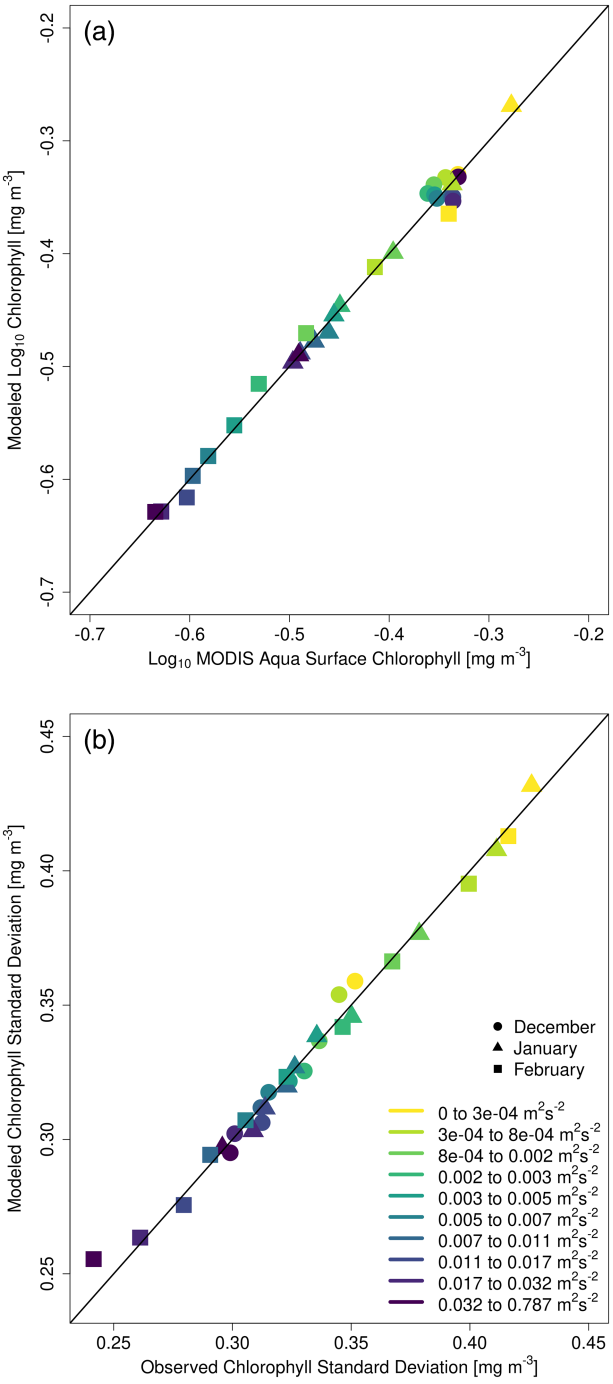

Figure 5. (a) Measured and predicted mean surface chlorophyll concentration from each of the 10 kinetic energy bins for each monthly model fit using equations (5) and (6). (b) Measured and predicted surface chlorophyll concentration standard deviation from each of the 10 kinetic energy bins for each monthly model fit using equations (5) and (6). Each different color represents 1 of the 10 kinetic energy bins. A 1:1 line is provided for reference.

CHL; it only makes it possible. This pattern is consistent with the expectation of an iron/light colimited system. Light levels, controlled through KE driven mixing, operate like a necessary, but not sufficient condition for phytoplankton bloom formation. Under favorable local light conditions, the delivery of iron through various processes leads to high CHL in the pelagic SO. The relationship between KE and CHL has a strong seasonal trend. As the pelagic SO emerges from seasonal light limitation in December, the probability of CHL > 1 mg m^{-3} is only slightly higher in low KE conditions. As the austral summer progresses, high CHL are much more likely in low KE conditions (Figure 3). These seasonal patterns may point toward the importance of regenerated iron (Tagliabue, Sallee, et al., 2014). One possible explanation is that as the austral summer progresses, the iron reservoir supplied by deep winter mixing is reduced, and the importance of diapycnal diffusion of iron into the mixed layer increases, favoring smaller phytoplankton cells over the larger bloom forming diatoms (Tagliabue, Sallee, et al., 2014). If this is the case, background concentrations of CHL would decrease through austral summer, which is consistent with the observations presented here (Figure 3).

4.2. The Kinetic Energy-Chlorophyll Probabilistic Model

The distributional KE-CHL relationship can be estimated statistically by mixing "background" and "bloom" normal distributions. Because the mean, standard deviation, and mixing percentage of these two distributions are themselves a function of KE (Figure 4), KE can be used to probabilistically predict CHL on monthly time scales. The monthly probabilistic models accurately reproduce the mean and standard deviation of the observed CHL distributions (Figure 5) and accurately reproduce the observed distributions in each of the 10 KE bin (Figure 6) for all summer months combined. When all of the monthly data are combined, the overall KE predicted and observed CHL means and standard deviations do not statistically differ from a 1:1 line.

The KE-CHL model was designed to predict a population of CHL pixels over time, rather than an individual pixel over time. However, if applied over pixels in space, and integrated over long time periods, it generally reproduces the climatological spatial patterns of CHL in the pelagic SO (Figure 7). Applied in this fashion, the KE-CHL model under predicts CHL on a pixel basis. This is because the KE-CHL model does not contain any information about the temporal or spatially autocorrelated nature of phytoplankton blooms. A pixel with a phytoplankton bloom in a 5-day composite from the satellite observations would likely still persist in the following 5-day composite and is therefore not independent. The KE-CHL model presented here does not take this into account. It is worth noting that using only OSCAR-derived KE as an input, the KE-CHL model was able to describe 30% of the spatial variability in all summer months combined. This indicates that KE has significant predictive power on the spatial distribution of CHL. The model performed the poorest in December, when KE had the weakest relationship with CHL (Figure 3a). The reasons for this will be explored in section 4.3. In January and February, the predicted spatial patterns of CHL based only on KE approximate the spatial patterns in the satellite-derived climatologies. Interestingly, the regions of higher predicted CHL are roughly coincident with the lowest phytoplankton iron utilization and highest putative levels of iron supply

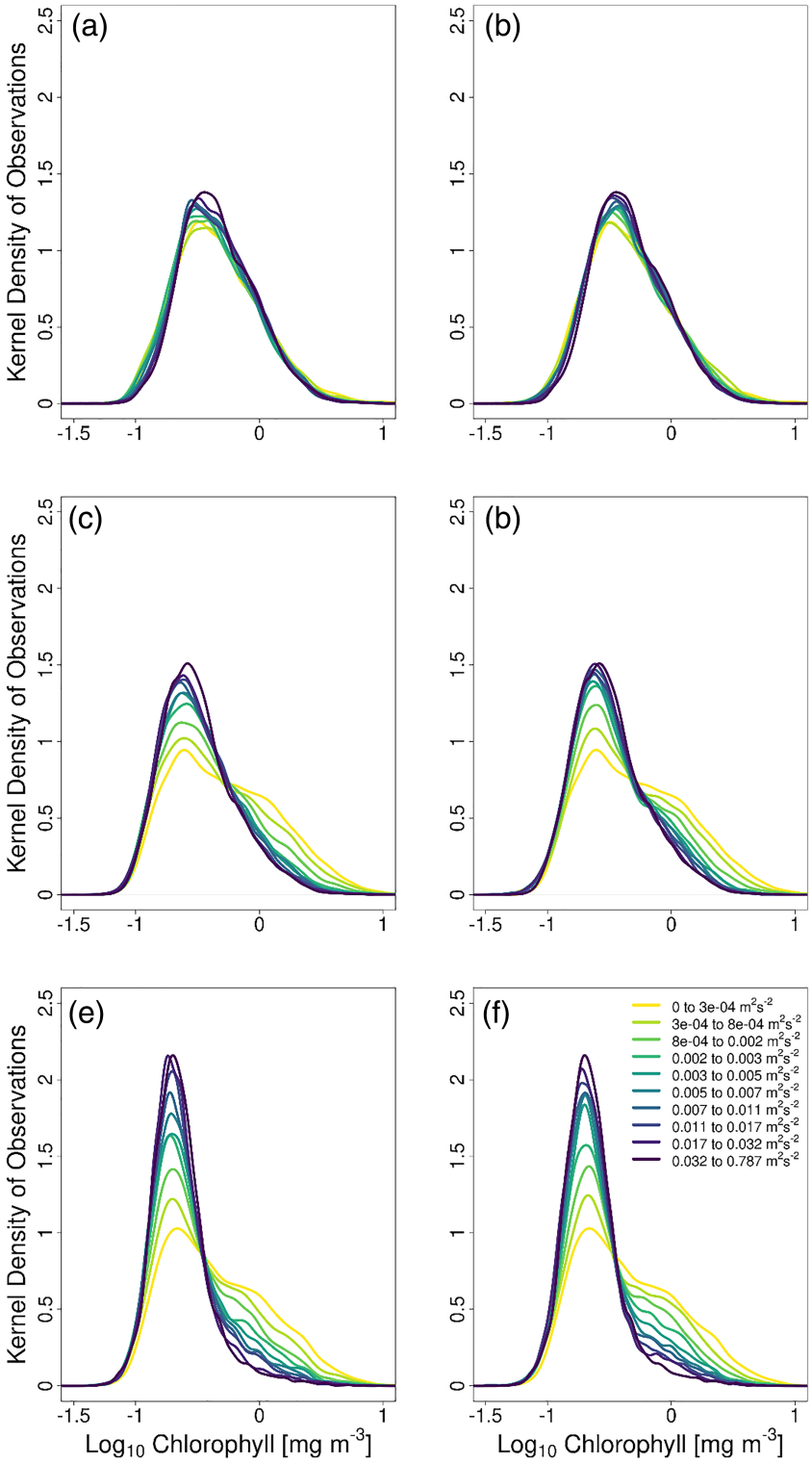

Figure 6. Left column: observed distributions of surface chlorophyll concentration in each of the 10 kinetic energy conditions (different colored lines) for the untrained 20% of the data by month (December = panel a; January = panel c; February = panel e). Right column: modeled distribution of surface chlorophyll concentration trained on 80% of the data by month and applied to the remaining 20% of data for each of the 10 kinetic energy conditions (December = panel b; January = panel d; February = panel f).

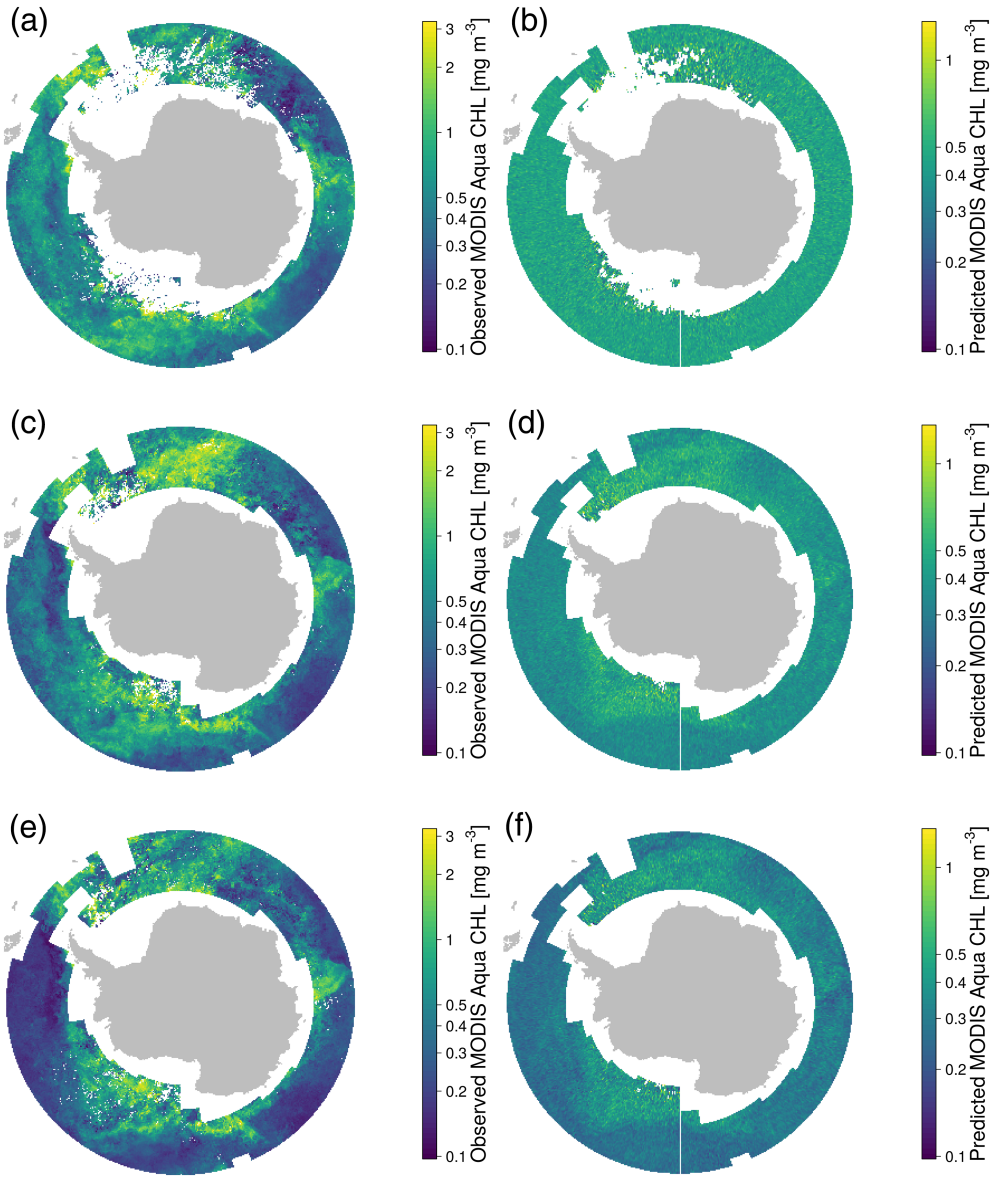

Figure 7. Climatology made from 5-day composites of MODIS-Aqua surface chlorophyll concentrations from 2003–2017 for December (a), January (c), and February (e). Climatology made from surface chlorophyll predictions from appropriate monthly models using 5-day composites of OSCAR surface current derived kinetic energy from 2003–2017 for December (b), January (d), and February (f).

(Figure 5 in Boyd et al., 2012). This is an expected result in relatively iron rich regions where, as we suggest, high KE is an indication of light limitation.

4.3. Kinetic Energy and MLD

In the SO, wind speeds have been shown to have an impact of mixing of surface waters and, consequently, phytoplankton concentration in the upper ocean (Carranza et al., 2018; Carranza & Gille, 2015). While wind speed is only one factor to consider for increased mixing, it is a major component of OSCAR surface currents (Bonjean & Lagerloef, 2002), so studies investigating the effect of wind speed on CHL can be used to provide context to this KE-CHL relationship. Both Carranza and Gille (2015) and Carranza et al. (2018) have shown that wind speed can be used as a proxy for mixing and high wind speeds on a daily to a synoptic storm scale can impact CHL. Carranza and Gille (2015) noted that increased wind speeds could actually transiently deepen the MLD and entrain Fe, resulting in increased CHL. Similarly, Carranza et al. (2018) found that

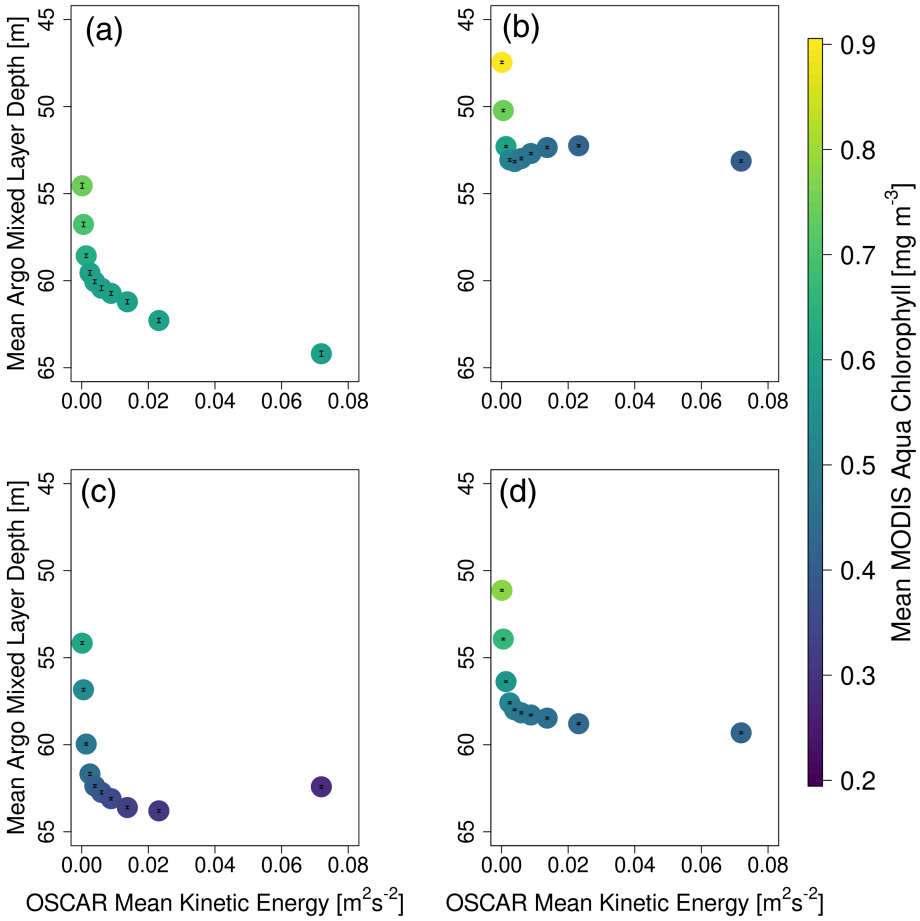

Figure 8. Climatological Argo float mixed layer depths from 2001–2006 matched to OSCAR surface current derived kinetic energy and colored by MODIS-Aqua surface chlorophyll concentration in December (a), January (b), February (c), and overall (d). The 10 points in each panel are generated according to the same 10% binning procedure as in Figure 3 where each dot contains 10% of the matched kinetic energy, surface chlorophyll concentration, and mixed layer depth data for a given month. Tick marks correspond with ±1 standard error of the mean. Note the different *y* axis from Figure 9.

increased winds corresponded with deeper MLDs with consistently smaller variance in CHL. Intermittent atmospheric forcing was found to impact CHL by allowing periods of reduced mixing between periods of increased winds (Carranza et al., 2018). This concept of variations in storm-driven mixing leading to increased CHL is similar to the concept of low KE as a necessary but not sufficient precondition for high CHL presented here.

The relationship between KE and CHL suggests that KE may be a proxy for light limitation by changing the mixing depth of phytoplankton. Because both MLD and euphotic depth range from 20–100 m during SO summers (Soppa et al., 2013), it is plausible that high KE limits phytoplankton growth by reducing their time spent in the euphotic zone. Figure 8 suggests that MLD derived from an Argo float climatology deepens with increased KE. Similar patterns, although not as smooth, are observed in CHL and MLD derived from SOCCOM floats (Figure 9). However, light limitation of phytoplankton is not the only explanation for the reduced CHL at higher KE and deeper MLD.

Higher KE and deeper MLD may simply lead to the dilution of CHL in the upper mixed layer, thus an apparent decrease in CHL. The deepening of the MLD increases the volume in which phytoplankton are distributed, thus diluting their concentrations if the newly entrained waters are phytoplankton free. Figures 8 and 9 can be used to test if a dilution effect explains this KE-CHL relationship. If dilution is a plausible explanation for the reduction in CHL, decreases in CHL should scale with a deepening mixed layer. In December, mean CHL was 0.73 mg m^{-3} with an average MLD of 54 m in the weakest KE bin (Figure 8a). This CHL, diluted

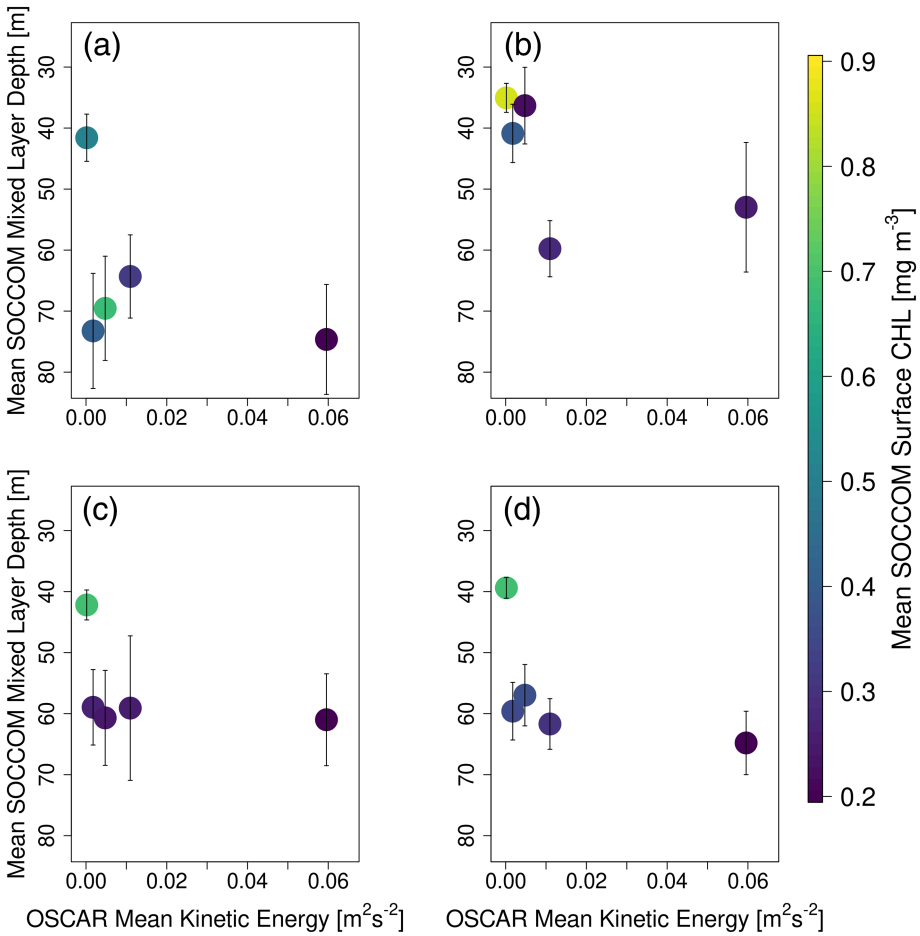

Figure 9. Compiled mixed layer depth from SOCCOM floats matched to OSCAR surface current derived kinetic energy and colored by SOCCOM float mean surface chlorophyll concentration in December (a), January (b), February (c), and all summer months combined (d). The 5 points in each panel are generated according to the same binning procedure as in Figure 3 but into 20% bins to compensate for the difference in the number of data points. Tick marks correspond with ±1 standard error of the mean. Note the different *y* axis from Figure 8.

over the 64-m mixed layer observed in the highest KE bin would result in an approximate concentration of 0.62 mg m^{-3}, which is only slightly higher than the CHL of 0.59 mg m^{-3} observed in this bin. In the in situ SOCCOM data, December CHL (0.5 mg m^{-3}) and MLD (41 m) diluted over the 74-m mixed layer observed in the highest KE bin results in an approximate concentration of 0.28 mg m^{-3}. This is slightly higher than the concentration of 0.19 mg m^{-3} observed in this bin (Figure 9a). Considering these two examples as rough, back-of-the-envelope calculations, a dilution effect is a plausible potential explanation behind this KE-CHL relationship in December. This may also explain why there are relatively small differences in CHL distributions with respect to KE in December (Figure 3a) and why the spatial prediction of CHL in December is poor (Figure 7a). However, a dilution effect does not seem plausible in January or February, as the CHL in the highest KE bins are about half the expected value if only dilution was responsible for CHL reductions at higher KE and deeper MLD. This suggests that higher KE in January and February likely leads deeper mixing, which creates a light light-limited environment for phytoplankton in the pelagic SO.

Our analysis shows the KE-CHL relationship is markedly different in December compared to both January and February (Figures 3, 8, and 9). On average, the observed bin mean CHL in December is higher than in January and February. In addition to dilution, the observed differences in December compared to January and February are likely due to the increasing seasonal availability of light, standing stock of macronutrients and micronutrients from deep winter mixing, and the consequent seasonal timing of phytoplankton blooms

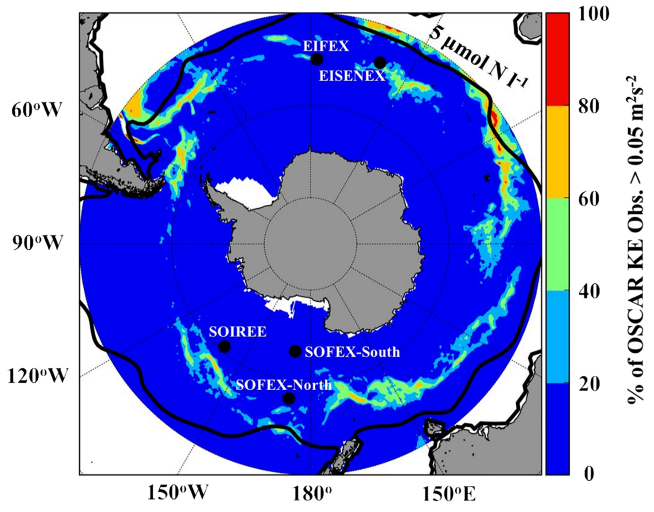

Figure 10. Frequency distributions of kinetic energy derived from OSCAR currents >0.05 m^2 s^{-2}. If high kinetic energy is a proxy for light limitation, regions of frequent high kinetic energy conditions may make it difficult to determine the impact of iron additions due to deep mixing conditions and the potential for light limitation.

throughout the SO (Thomalla et al., 2011). In December, KE has less of an effect on phytoplankton abundance because as light becomes seasonally available, phytoplankton will utilize the available nutrients, thus leaving a more nutrient (iron) limited environment in January and February (Tagliabue, Aumont, et al., 2014). These potential explanations are in agreement with biofloat observations in the Drake Passage (Davies et al., 2019). A float profiling at high-frequency (2-day rather than 10-day cycle) observed low KE precedes a bloom followed by increasing KE leading to potential dilution within an eddy-driven subduction event (Davies et al., 2019).

4.4. Relevance to Iron Fertilization Experiments

The KE-CHL probabilistic relationship described here implies there may be regions of the SO that are unlikely to support phytoplankton blooms because of consistently high KE, even if other limiting factors such as iron are alleviated. Because low KE (<0.05 m^2 s^{-2}) during January and February seems to be a precondition for high CHL, regions of consistently high KE could also be unsuitable for large-scale iron fertilization experiments. It appears that the successful large-scale iron addition experiments (i.e., experiments where Fe addition generated an increase in CHL) were conducted in low KE environments (Table S2). Regions with average values greater than ~0.05 m^2 s^{-2} in Figure 1b may present challenges for detecting the effect of iron addition because of potentially unfavorable light conditions (Figure 10). Additionally, this suggests that both past and future states of SO circulation are important for understanding the potential of the SO to draw down atmospheric carbon.

5. Conclusion

This study shows that KE is a proxy for light limitation during austral summer and that low KE behaves like a necessary but not sufficient condition for high CHL. We interpret this relationship to be consistent with a colimiting relationship between local light availability mediated through mixing and variable iron supply from multiple sources. With only KE as an input, probabilistic models are able to describe 30% of the CHL spatial distribution, indicating that mesoscale light limitation is likely a significant regulator of CHL in the austral summer in the pelagic SO.

Several studies estimate that the SO could account for anywhere from a tenth to a quarter of the annual global ocean carbon uptake (Mcneil & Matear, 2007; Roy et al., 2003; Takahashi et al., 2002). Over the next century, SO surface waters are expected to experience increased warming, shallowing of MLDs, increases in light, and changes in upwelling and nutrient fluxes (Deppeler & Davidson, 2017). As a result, phytoplankton productivity is expected to increase, and the biological pump in the SO is expected to have a larger role in carbon sequestration (Gregg & Rousseaux, 2014; Sarmiento et al., 1998). However, these projections do not consider subseasonal, suppression of CHL due to KE effects discussed here. The recreation of the KE-CHL relationships shown here could serve as a qualitative check for modeling studies attempting to quantify the interaction between CHL, light, MLD, and iron in the pelagic SO.

Acknowledgments
Remote sensing reflectance from the Moderate Imaging Spectroradiometer (MODIS) *Aqua* satellite used to derived CHL estimates were collected and made publicly available by the National Aeronautics and Space Administration (NASA) (at 10.5067/AQUA/MODIS/L3B/RRS/2018). Surface currents were modeled by the Ocean Surface Current Analysis Real-Time (OSCAR) product and made publicly available by the National Oceanic and Atmospheric Administration (NOAA, at https://podaac.jpl.nasa.gov/dataset/OSCAR_L4_OC_third-deg). Data were collected and made freely available by the Southern Ocean Carbon and Climate Observations and Modeling (SOCCOM) Project funded by the National Science Foundation, Division of Polar Programs (NSF PLR -1425989), supplemented by NASA, and by the International Argo Program and the NOAA programs that contribute to it. The Argo Program is part of the Global Ocean Observing System (http://doi.org/10.17882/42182). A monthly mixed layer depth climatology was provided by Dong et al. (20082008) (at https://doi.org/10.1029/2006JC004051). Funding provided by the University of Delaware Marian R. Okie Fellowship. A special thanks to Dr. Matthew Oliver for his guidance and advice and the rest of the Orb Lab for their daily support.

References

Arrigo, K. R., Van Dijken, G. L., & Bushinsky, S. (2008). Primary production in the Southern Ocean, 1997–2006. *Journal of Geophysical Research*, *113*, C08004. https://doi.org/10.1029/2007JC004551

Atlas, R., Hoffman, R. N., Bloom, S. C., Jusem, J. C., & Ardizzone, J. (1996). A multiyear global surface wind velocity dataset using SSM/I wind observations. *Bulletin of the American Meteorological Society*, *77*(5), 869–882. https://doi.org/10.1175/1520-0477(1996)077<0869:AMGSWV>2.0.CO;2

Behrenfeld, M. J. (2010). Abandoning Sverdrup's critical depth hypothesis on phytoplankton blooms. *Ecology*, *91*(4), 977–989. https://doi.org/10.1890/09-1207.1

Benaglia, T., Chauveau, D., Hunter, D., & Young, D. (2009). Mixtools: An R package for analyzing finite mixture models. *Journal of Statistical Software*, *32*(6), 1–29. https://doi.org/10.18637/jss.v032.i06

Blain, S., Queguiner, B., Armand, L., Belviso, S., Bombled, B., Bopp, L., et al. (2007). Effect of natural iron fertilization on carbon sequestration in the Southern Ocean. *Nature*, *446*(7139), 1070–1074. https://doi.org/10.1038/nature05700

Blain, S., Treguer, P., & Belviso, S. (2001). A biogeochemical study of the island mass effect in the context of the iron hypothesis: Kerguelen Islands, Southern Ocean. *Deep Sea Research, Part I*, *48*(1), 163–187. https://doi.org/10.1016/S0967-0637(00)00047-9

Bonjean, F., & Lagerloef, G. S. E. (2002). Diagnostic model and analysis of the surface currents in the tropical Pacific Ocean. *Journal of Physical Oceanography*, *32*(10), 2938–2954. https://doi.org/10.1175/1520-0485(2002)032<2938:DMAAOT>2.0.CO;2

Boyd, P. W., Arrigo, K. R., Strzepek, R., & Van Dijken, G. L. (2012). Mapping phytoplankton iron utilization: Insights into Southern Ocean supply mechanisms. *Journal of Geophysical Research*, *117*, C06009. https://doi.org/10.1029/2011JC007726

Boyd, P. W., & Ellwood, M. J. (2010). The biogeochemical cycle of iron in the ocean. *Nature Geoscience*, *3*(10), 675–682. https://doi.org/10.1038/ngeo964

Boyd, P. W., Watson, A. J., Law, C. S., Abraham, E. R., Trull, T., Murdoch, R., et al. (2000). A mesoscale phytoplankton bloom in the polar southern ocean stimulated by iron fertilization. *Nature*, *407*(6805), 695–702. https://doi.org/10.1038/35037500

Carranza, M. M., & Gille, S. T. (2015). Southern Ocean wind-driven entrainment enhances satellite chlorophyll-a through the summer. *Journal of Geophysical Research: Oceans*, *120*, 304–323. https://doi.org/10.1002/2014JC010203

Carranza, M. M., Gille, S. T., Franks, P. J., Johnson, K. S., Pinkel, R., & Girton, J. B. (2018). When mixed layers are not mixed, Storm-driven mixing and bio-optical vertical gradients in mixed layers of the Southern Ocean. *Journal of Geophysical Research: Oceans*, *123*, 7264–7289. https://doi.org/10.1029/2018JC014416

Chelton, D. B., Schlax, M. G., Samelson, R. M., & de Szoeke, R. A. (2007). Global observations of large oceanic eddies. *Geophysical Research Letters*, *34*, L15606. https://doi.org/10.1029/2007GL030812

Coale, K. H., Johnson, K. S., Chavez, F. P., Buesseler, K. O., Barber, R. T., Brzezinski, M. A., et al. (2004). Southern Ocean iron enrichment experiment: Carbon cycling in high-and low-Si waters. *Science*, *304*(5669), 408–414. https://doi.org/10.1126/science.1089778

Comiso, J. C., McClain, C. R., Sullivan, C. W., Ryan, J. P., & Leonard, C. L. (1993). Coastal zone color scanner pigment concentrations in the Southern Ocean and relationships to geophysical surface features. *Journal of Geophysical Research*, *98*(C2), 2419–2451. https://doi.org/10.1029/92JC02505

Cota, G. F., Harrison, W. G., Platt, T., Sathyendranath, S., & Stuart, V. (2003). Bio-optical properties of the Labrador Sea. *Journal of Geophysical Research*, *108*(C7), 3228. https://doi.org/10.1029/2000JC000597

Daniault, N., & Ménard, Y. (1985). Eddy kinetic energy distribution in the Southern Ocean from altimetry and FGGE drifting buoys. *Journal of Geophysical Research*, *90*(C6), 11,877–11,889. https://doi.org/10.1029/JC090iC06p11877

Davies, A. R., Veron, F., & Oliver, M. J. (2019). Biofloat observations of a phytoplankton bloom and carbon export in the Drake Passage. *Deep Sea Research Part I: Oceanographic Research Papers.*, *146*, 91–102. https://doi.org/10.1016/j.dsr.2019.02.004

De Baar, H. J. W., Boyd, P. W., Coale, K. H., Landry, M. R., Tsuda, A., Assmy, P., et al. (2005). Synthesis of iron fertilization experiments: From the iron age in the age of enlightenment. *Journal of Geophysical Research*, *110*, C09S16. https://doi.org/10.1029/2004JC002601

Deppeler, S. L., & Davidson, A. T. (2017). Southern Ocean phytoplankton in a changing climate. *Frontiers in Marine Science*, *4*, 40. https://doi.org/10.3389/fmars.2017.00040

Dierssen, H. M., & Smith, R. C. (2000). Bio-optical properties and remote sensing ocean color algorithms for Antarctic Peninsula waters. *Journal of Geophysical Research*, *105*(C11), 26,301–26,312. https://doi.org/10.1029/1999JC000296

Dong, S., Sprintall, J., Gille, S. T., & Talley, L. (2008). Southern Ocean mixed-layer depth from Argo float profiles. *Journal of Geophysical Research*, *113*, C06013. https://doi.org/10.1029/2006JC004051

El-Sayed, S. Z., Biggs, D. C., & Holm-Hansen, O. (1983). Phytoplankton standing crop, primary productivity, and near-surface nitrogenous nutrient fields in the Ross Sea, Antarctica. *Deep-Sea Research 1*, *30*(8), 871–886. https://doi.org/10.1016/0198-0149(83)90005-5

Esaias, W. E., Abbott, M. R., Barton, I., Brown, O. B., Campbell, J. W., Carder, K. L., et al. (1998). An overview of MODIS capabilities for ocean science observations. *IEEE Transactions on Geoscience and Remote Sensing*, *36*(4), 1250–1265. https://doi.org/10.1109/36.701076

Fitch, D. T., & Moore, J. K. (2007). Wind speed influence on phytoplankton bloom dynamics in the Southern Ocean Marginal Ice Zone. *Journal of Geophysical Research*, *112*, C08006. https://doi.org/10.1029/2006JC004061

Gervais, F., Riebesell, U., & Gorbunov, M. Y. (2002). Changes in primary productivity and chlorophyll a in response to iron fertilization in the Southern Polar Frontal Zone. *Limnology and Oceanography*, *47*(5), 1324–1335. https://doi.org/10.4319/lo.2002.47.5.1324

Gray, A. R., Johnson, K. S., Bushinsky, S. M., Riser, S. C., Russell, J. L., Talley, L. D., et al. (2018). Autonomous biogeochemical floats detect significant carbon dioxide outgassing in the high-latitude Southern Ocean. *Journal of Geophysical Research: Oceans*, *45*, 9049–9057. https://doi.org/10.1029/2018GL078013

Gregg, W. W., & Casey, N. W. (2004). Global and regional evaluation of the SeaWiFS chlorophyll data set. *Remote Sensing of Environment*, *93*(4), 463–479. https://doi.org/10.1016/j.rse.2003.12.012

Gregg, W. W., & Rousseaux, C. S. (2014). Decadal trends in global pelagic ocean chlorophyll: A new assessment integrating multiple satellites, in situ data, and models. *Journal of Geophysical Research: Oceans*, *119*, 5921–5933. https://doi.org/10.1002/2014JC010158

Gruber, N., Gloor, M., Mikaloff Fletcher, S. E., Doney, S. C., Dutkiewicz, S., Follows, M. J., et al. (2009). Oceanic sources, sinks, and transport of atmospheric CO2. *Global Biogeochemical Cycles*, *23*, GB1005. https://doi.org/10.1029/2008GB003349

Haëntjens, N., Boss, E., & Talley, L. D. (2017). Revisiting Ocean Color algorithms for chlorophyll a and particulate organic carbon in the Southern Ocean using biogeochemical floats. *Journal of Geophysical Research: Oceans*, *122*, 6583–6593. https://doi.org/10.1002/2017JC012844

Hoffmann, L., Peeken, I., & Lochte, K. (2007). Effects of iron on the elemental stoichiometry during EIFEX and in the diatoms Fragilariopsis kerguelensis and Chaetoceros dichaeta. *Biogeosciences (BG)*, *4*(4), 569–579. https://doi.org/10.5194/bg-4-569-2007

Holeton, C. L., Ne'de'lec, F., Sanders, R., Brown, L., Moore, C. M., Stevens, D. P., et al. (2005). Physiological state of phytoplankton communities in the southwest Atlantic sector of the Southern Ocean, as measured by fast repetition rate fluorometry. *Polar Biology*, *29*(1), 44–52. https://doi.org/10.1007/s00300-005-0028-y

Holm-Hansen, O., Kahru, M., & Hewes, C. D. (2005). Deep chlorophyll a maxima (DCMs) in pelagic Antarctic waters in relation to bathymetric features and dissolved iron concentrations. *Marine Ecology Progress Series*, *297*, 71–81. https://doi.org/10.3354/meps297071

Johnson, K. S., Plant, J. N., Coletti, L. J., Jannasch, H. W., Sakamoto, C. M., Riser, S. C., et al. (2017). Biogeochemical sensor performance in the SOCCOM profiling float array. *Journal of Geophysical Research: Oceans*, *122*, 6416–6436. https://doi.org/10.1002/2017JC012838

Johnson, R., Strutton, P. G., Wright, S. W., Mcminn, A., & Meiners, K. M. (2013). Three improved satellite chlorophyll algorithms for the Southern Ocean. *Journal of Geophysical Research: Oceans*, *118*, 3694–3703. https://doi.org/10.1002/jgrc.20270

Kahru, M., & Mitchell, B. G. (1999). Empirical chlorophyll algorithm and preliminary SeaWiFS validation for the California current. *International Journal of Remote Sensing*, *20*(17), 3423–3429. https://doi.org/10.1080/014311699211453

Klunder, M. B., Laan, P., Baar, H. J. W. D., Middag, R., Neven, I., & Ooijen, J. V. (2014). Dissolved Fe across the Weddell Sea and Drake Passage: Impact of DFe on nutrient uptake. *Biogeosciences*, *11*(3), 651–669. https://doi.org/10.5194/bg-11-651-2014

Large, W. G., & Pond, S. (1981). Open ocean momentum flux measurements in moderate to strong winds. *Journal of Physical Oceanography*, *11*(3), 324–336. https://doi.org/10.1175/1520-0485(1981)011<0324:OOMFMI>2.0.CO;2
Legendre, P. (2014). Model II regression. *R package version 1.7-2/r2858.* https://R-Forge.R-project.org/projects/vegan/
Martin, J. H. (1990). Glacial-interglacial CO_2 change: The iron hypothesis. *Paléo*, *5*, 1–13.
Mcneil, B. I., & Matear, R. J. (2007). Climate change feedbacks on future oceanic acidification. *Tellus Series B: Chemical and Physical Meteorology*, *59*(2), 191–198. https://doi.org/10.1111/j.1600-0889.2006.00241.x
Moore, J. K., & Abbott, M. R. (2000). Phytoplankton chlorophyll distributions and primary production in the Southern Ocean. *Journal of Geophysical Research*, *105*(C12), 28,709–28,722. https://doi.org/10.1029/1999JC000043
Nolting, R. F., Baar, H. J. W. D., Bennekom, A. J. V., & Masson, A. (1991). Cadmium, copper and iron in the Scotia Sea, Weddell Sea and Weddell/Scotia Confluence (Antarctica). *Marine Chemistry*, *35*(14), 219–243. https://doi.org/10.1016/S0304-4203(09)90019-6
R Development Core Team (2017). *R: A language and environment for statistical computing*. Vienna, Austria: R Foundation for Statistical Computing.
Roy, T., Rayner, P., Matear, R., & Francey, R. (2003). Southern Hemisphere ocean CO2 uptake: Reconciling atmospheric and oceanic estimates. *Tellus Series B: Chemical and Physical Meteorology*, *55*(2), 701–710. https://doi.org/10.3402/tellusb.v55i2.16749
Sarmiento, J. L., Hughes, T. M. C., Stouffer, R. J., & Manabe, S. (1998). Simulated response of the ocean carbon cycle to anthropogenic climate warming. *Nature*, *393*(6682), 245–249. https://doi.org/10.1038/30455
Smetacek, V., Klaas, C., Strass, V. H., Assmy, P., Montresor, M., Cisewski, B., et al. (2012). Deep carbon export from a Southern Ocean iron-fertilized diatom bloom. *Nature*, *487*(7407), 313–319. https://doi.org/10.1038/nature11229
Smith, K. L. Jr., Robison, B. H., Helly, J. J., Kaufmann, R. S., Ruhl, H. A., Shaw, T. J., et al. (2007). Free-drifting icebergs: Hot spots of chemical and biological enrichment in the Weddell Sea. *Science*, *317*(5837), 478–482. https://doi.org/10.1126/science.1142834
Sokolov, S., & Rintoul, S. R. (2007). On the relationship between fronts of the Antarctic Circumpolar Current and surface chlorophyll concentrations in the Southern Ocean. *Journal of Geophysical Research*, *112*, C07030. https://doi.org/10.1029/2006JC004072
Song, H. M., Long, M. C., Gaude, P., Frenger, I., Marshall, J., & McGillicuddy, D. J. Jr. (2018). Seasonal variation in the correlation between anomalies in sea level and chlorophyll in the Antarctic Circumpolar Current region. *Geophysical Research Letters*, *45*(10), 5011–5019. https://doi.org/10.1029/2017GL076246
Soppa, M. A., Dinter, T., Taylor, B. B., & Bracher, A. (2013). Satellite derived euphotic depth in the Southern Ocean: Implications for primary production modelling. *Remote Sensing of Environment*, *137*, 198–211. https://doi.org/10.1016/j.rse.2013.06.017
Strutton, P. G., Martz, T. R., Degrandpre, M. D., Mcgillis, W. R., Drennan, W. M., & Boss, E. (2011). Bio-optical observations of the 2004 Labrador Sea phytoplankton bloom. *Journal of Geophysical Research*, *116*, C11037. https://doi.org/10.1029/2010JC006872
Tagliabue, A., Aumont, O., & Bopp, L. (2014). The impact of different external sources of iron on the global carbon cycle. *Geophysical Research Letters*, *41*, 920–926. https://doi.org/10.1002/2013GL059059
Tagliabue, A., Sallee, J. B., Bowie, A. R., Levy, M., Swart, S., & Boyd, P. W. (2014). Surface water iron supplies in the Southern Ocean sustained by deep winter mixing. *Nature*, *7*, 314–320. https://doi.org/10.1038/ngeo2101
Takahashi, T., Sutherland, S. C., Sweeney, C., Poisson, A., Metzl, N., Tilbrook, B., et al. (2002). Global sea-air CO2 flux based on climatological surface ocean pCO(2), and seasonal biological and temperature effects. *Deep-Sea Research Part II-Topical Studies in Oceanography*, *49*(9–10), 1601–1622. https://doi.org/10.1016/S0967-0645(02)00003-6
Thomalla, S. J., Fauchereau, N., Swart, S., & Monteiro, P. M. S. (2011). Regional scale characteristics of the seasonal cycle of chlorophyll in the Southern Ocean. *Biogeosciences*, *8*(10), 2849–2866. https://doi.org/10.5194/bg-8
Uchida, T., Balwada, D., Abernathey, R., McKinley, G., Smith, S., & Lévy, M. (2019). The contribution of submesoscale over mesoscale eddy iron transport in the open Southern Ocean. *Journal of Advances in Modeling Earth Systems*, *11*(12), 3934–3958. https://doi.org/10.1029/2019MS001805
Venables, H., & Moore, C. M. (2010). Phytoplankton and light limitation in the Southern Ocean: Learning from high-nutrient, high-chlorophyll areas. *Journal of Geophysical Research*, *115*, C02015. https://doi.org/10.1029/2009JC005361
Venables, H. J., Pollard, R. T., & Popova, E. E. (2007). Physical conditions controlling the development of a regular phytoplankton bloom north of the Crozet Plateau, Southern Ocean. *Deep-Sea Research: Part II*, *54*(18-20), 1949–1965. https://doi.org/10.1016/j.dsr2.2007.06.014